mass movements, often show associated spectral differences. For example, the Oppia region's surface exhibits variations in albedo and spectral slope that indicate differences in surface materials (Fig. 4A). Moreover, the area around the (Fig. 3) fresh Oppia crater (E) and the crater floor (F) have shallower BI depths (Fig. 4B), revealing material poorer in pyroxene. The cratering process here results in inverted stratigraphy of roughly the upper third of the target lithology in the ejecta blanket nearest the rim [e.g., (*29*)]. The crater floor and material partway up the walls have a reddish hue similar to the ejecta just outside the rim, consistent with the lower layers in this crater being composed of rock poorer in pyroxene. The cyan color indicates that the soils just below the rim (H) have stronger BI absorption and thus have higher pyroxene content or different grain size (Fig. 4C). The small crater (S) is surrounded by a halo of bright and green materials, similar to the layer exposed in Oppia (H), suggesting a similar composition. VIR thus reveals that the Oppia impact exposed different kinds of materials, suggesting complex, small-scale crustal stratigraphy on Vesta.

At all scales, pyroxene absorptions are the most prominent spectral features on Vesta and, on average, the spectral parameters of Vesta resemble those of howardites (fig. S5). The VIR spectra are thus consistent with a surface covered by a howardite-like regolith containing varying proportions of eucrite and diogenite at different locations. This firmly supports the link between Vesta and the HEDs, providing geologic context for these samples, which furthers our understanding of the formation and evolution of Vesta.

Furthermore, Vesta exhibits large color and spectral variations that often reflect geological structures, indicating a complex geological and evolutionary history, more similar to that of the terrestrial planets than to other asteroids visited by spacecraft (*17*, *18*). The occurrence of a greater proportion of diogenite at depth is a critical finding, not demonstrated by data from the Hubble Space Telescope or telescopic observations (*30*, *31*), and broadly consistent with magma ocean models for Vesta's differentiation. On the other hand, the fact that mixtures of diogenite and eucrite appear ubiquitous in all regions, coupled with the occurrence of smaller-scale variations in mineralogy, make it premature to distinguish between a simple layered crust of eucrite and underlying diogenite (*32*) or a complex eucrite crust with intruded diogenitic plutons (*14*). The Dawn mission provides the first spatially detailed view of the distribution of the rock types, allowing insight into the magmatic processes that formed the solar system's "smallest planet."

References and Notes

1. T. B. McCord, J. B. Adams, T. V. Johnson, *Science* **168**, 1445 (1970).
2. M. A. Feierberg, M. J. Drake, *Science* **209**, 805 (1980).
3. G. J. Consolmagno, M. J. Drake, *Geochim. Cosmochim. Acta* **41**, 1271 (1977).
4. M. J. Drake, In *Asteroids*, T. Gehrels, Ed. (Univ. Arizona Press, Tucson, AZ, 1979), pp. 765–782
5. R. P. Binzel *et al.*, *Icarus* **128**, 95 (1997).
6. M. C. De Sanctis *et al.*, *Astron. Astrophys.* **533**, A77 (2011).
7. N. A. Moscovitz *et al.*, *Icarus* **208**, 773 (2010).
8. M. C. De Sanctis *et al.*, *Mon. Not. R. Astron. Soc.* **412**, 2318 (2011).
9. K. Righter, M. J. Drake, *Meteorit. Planet. Sci.* **32**, 929 (1997).
10. P. H. Warren, *Meteorit. Planet. Sci.* **32**, 945 (1997).
11. R. C. Greenwood, I. A. Franchi, A. Jambon, P. C. Buchanan, *Nature* **435**, 916 (2005).
12. D. W. Mittlefehldt *et al.*, in *Planetary Materials: Reviews in Mineralogy 36*, J. J. Papike, Ed. (Mineralogical Society of America, Chantilly, VA, 1998), pp. 4-1–4-195.
13. A. Beck, H. Y. McSween Jr., *Meteorit. Planet. Sci.* **45**, 850 (2010).
14. J.-A. Barrat, A. Yamaguchi, B. Zanda, C. Bollinger, M. Bohn, *Geochim. Cosmochim. Acta* **74**, 6218 (2010).
15. M. C. De Sanctis *et al.*, *Space Sci. Rev.* (2010).
16. C. T. Russell *et al.*, *Science* **336**, 684 (2012).
17. A. Coradini *et al.*, *Science* **334**, 492 (2011).
18. J. Veverka *et al.*, *Science* **289**, 2088 (2000).
19. R. G. Burns, *Mineralogical Applications of Crystal Field Theory* (Cambridge Univ. Press, Cambridge, 1993).
20. L. A. McFadden, T. B. McCord, C. Pieters, *Icarus* **31**, 439 (1977).
21. P. Schenk *et al.*, *Science* **336**, 694 (2012).
22. R. Jaumann *et al.*, *Science* **336**, 687 (2012).
23. S. Marchi *et al.*, *Science* **336**, 690 (2012).
24. P. H. Warren, G. W. Kallemeyn, H. Huber, F. Ulff-Møller, W. Choe, *Geochim. Cosmochim. Acta* **73**, 5918 (2009).
25. L. Wilkening, D. Lal, A. M. Reid, *Earth Planet. Sci. Lett.* **10**, 334 (1971).
26. M. J. Gaffey, *J. Geophys. Res.* **81**, 905 (1976).
27. L. E. Bowman, M. N. Spilde, J. J. Papike, *Meteorit. Planet. Sci.* **32**, 869 (1997).
28. J. S. Delaney, M. Prinz, H. Takeda, *J. Geophys. Res.* **89**, (suppl.), C251 (1984).
29. H. J. Melosh, *Impact Cratering: A Geologic Process* (Oxford Univ. Press, Oxford, 1989).
30. Telescopic data suggested a prominent diogenite region. In the adopted coordinate system, this diogenite spot was moved to the northern hemisphere, where VIR does not find this evidence.
31. J. Y. Li *et al.*, *Icarus* **208**, 238 (2010).
32. H. Takeda, *Icarus* **40**, 455 (1979).

Acknowledgments: VIR is funded by the Italian Space Agency and was developed under the leadership of INAF-Istituto di Astrofisica e Planetologia Spaziali, Rome, Italy. The instrument was built by Selex-Galileo, Florence, Italy. The authors acknowledge the support of the Dawn Science, Instrument, and Operations Teams. This work was supported by the Italian Space Agency, and NASA's Dawn at Vesta Participating Scientists Program. A portion of this work was performed at the Jet Propulsion Laboratory under contract with NASA.

Supplementary Materials

www.sciencemag.org/cgi/content/full/336/6082/697/DC1
Supplementary Text
Figs. S1 to S5
Table S1

17 January 2012; accepted 16 April 2012
10.1126/science.1219270

Color and Albedo Heterogeneity of Vesta from Dawn

Vishnu Reddy,[1,2]* Andreas Nathues,[1] Lucille Le Corre,[1] Holger Sierks,[1] Jian-Yang Li,[3] Robert Gaskell,[4] Timothy McCoy,[5] Andrew W. Beck,[5] Stefan E. Schröder,[1] Carle M. Pieters,[6] Kris J. Becker,[7] Bonnie J. Buratti,[8] Brett Denevi,[9] David T. Blewett,[9] Ulrich Christensen,[1] Michael J. Gaffey,[2] Pablo Gutierrez-Marques,[1] Michael Hicks,[8] Horst Uwe Keller,[10] Thorsten Maue,[1] Stefano Mottola,[11] Lucy A. McFadden,[12] Harry Y. McSween,[13] David Mittlefehldt,[14] David P. O'Brien,[4] Carol Raymond,[8] Christopher Russell[15]

Multispectral images (0.44 to 0.98 μm) of asteroid (4) Vesta obtained by the Dawn Framing Cameras reveal global color variations that uncover and help understand the north-south hemispherical dichotomy. The signature of deep lithologies excavated during the formation of the Rheasilvia basin on the south pole has been preserved on the surface. Color variations (band depth, spectral slope, and eucrite-diogenite abundance) clearly correlate with distinct compositional units. Vesta displays the greatest variation of geometric albedo (0.10 to 0.67) of any asteroid yet observed. Four distinct color units are recognized that chronicle processes—including impact excavation, mass wasting, and space weathering—that shaped the asteroid's surface. Vesta's color and photometric diversity are indicative of its status as a preserved, differentiated protoplanet.

The Dawn spacecraft rendezvoused with the asteroid Vesta on 16 July 2011, and the Framing Cameras (FCs) (*1*) acquired images in seven colors (0.44 to 0.98 μm) and one broadband clear filter, mapping the entire sun-lit surface at a detail of ~9 to ~0.016 km/pixel. We used

[1]Max Planck Institute for Solar System Research, Max-Planck-Strasse 2, 37191 Katlenburg-Lindau, Germany. [2]Department of Space Studies, University of North Dakota, Grand Forks, ND 58202, USA. [3]Department of Astronomy, University of Maryland, College Park, MD 20742, USA. [4]Planetary Science Institute, 1700 East Fort Lowell, Suite 106, Tucson, AZ 85719, USA. [5]Department of Mineral Sciences, Smithsonian National Museum of Natural History, 10th and Constitution NW, Washington, DC 20560–0119, USA. [6]Department of Geological Sciences, Brown University, Providence, RI 02912, USA. [7]Astrogeology Science Center, U.S. Geological Survey, Flagstaff, AZ 86001, USA. [8]Jet Propulsion Laboratory, California Institute of Technology, 4800 Oak Grove Drive, Pasadena, CA 91109, USA. [9]Johns Hopkins University Applied Physics Laboratory, Laurel, MD 20723, USA. [10]Institut für Geophysik und extraterrestrische Physik, TU Braunschweig Mendelssohnstrasse 3, DE 38106 Braunschweig, Germany. [11]Deutsches Zentrum für Luft und Raumfahrt (DLR)–German Aerospace Center, Institute of Planetary Research, Rutherfordstrasse 2, D-12489 Berlin, Germany. [12]NASA/Goddard Space Flight Center, Mail Code 160, Greenbelt, MD 20771, USA. [13]Department of Earth and Planetary Sciences, University of Tennessee, 1412 Circle Drive, Knoxville, TN 37996–1410, USA. [14]Astromaterials Research Office, NASA Johnson Space Center, Mail Code KR, Houston, TX 77058, USA. [15]Institute of Geophysics and Planetary Physics, University of California Los Angeles, Los Angeles, CA 90024–1567, USA.

*To whom correspondence should be sent. E-mail: reddy@mps.mpg.de

these images to determine the global color characteristics and compositional heterogeneity of the asteroid's surface. The diversity of collected meteorites indicates that in the early solar system, the main asteroid belt held more than 100 large asteroids that were partially or totally melted but subsequently destroyed by collisions (*2*). Today, Vesta is the only surviving silicate-rich differentiated object (*3*). Two major goals of the Dawn mission are to help answer why Vesta is the only remaining member of this class and to use its history to understand terrestrial planet formation.

Vesta is the likely parent body of the howardite-eucrite-diogenite (HED) meteorites. Eucrites are crustal basalts, petrologically similar to terrestrial basalts; diogenites are ultramafic cumulates, likely formed in the lower crust of the asteroid; and howardites are physical mixtures (regolith) of eucrites and diogenites formed by impact processes. Spectroscopic (*4*) and petrologic evidence (*5*) originally suggested a HED-Vesta link, and the 3:1 mean-motion resonance with Jupiter at 2.5 AU could provide a pathway for pieces ejected from Vesta to near-Earth space (*6*). This connection was further solidified by the detection of the "Vestoids," a group of smaller (<10 km) asteroids that are spectrally similar to Vesta and span the orbital region between Vesta and the 3:1 resonance (*7*).

We converted the FC images to reflectance (I/F) by dividing the observed radiance by the solar irradiance from a normally solar-illuminated Lambertian disk, photometrically corrected to standard viewing geometry (30° incidence and 0° emergence and 30° phase angles). This was accomplished by using Hapke functions derived from disk-integrated ground-based telescopic observations of Vesta and Vestoids, as well as resolved data from the approach phase of the mission (*8*). A fit of the Dawn survey data in the wideband clear filter to Hapke's model yields fits to the Hapke parameters of 0.52 for the single scattering albedo (SSA), −0.29 for the backscattering parameter (confirming that Vesta's surface is backscattering as other asteroids are), and 20° for the mean slope angle defining macroscopic roughness. For each color acquisition, subpixel coregistration was accomplished to

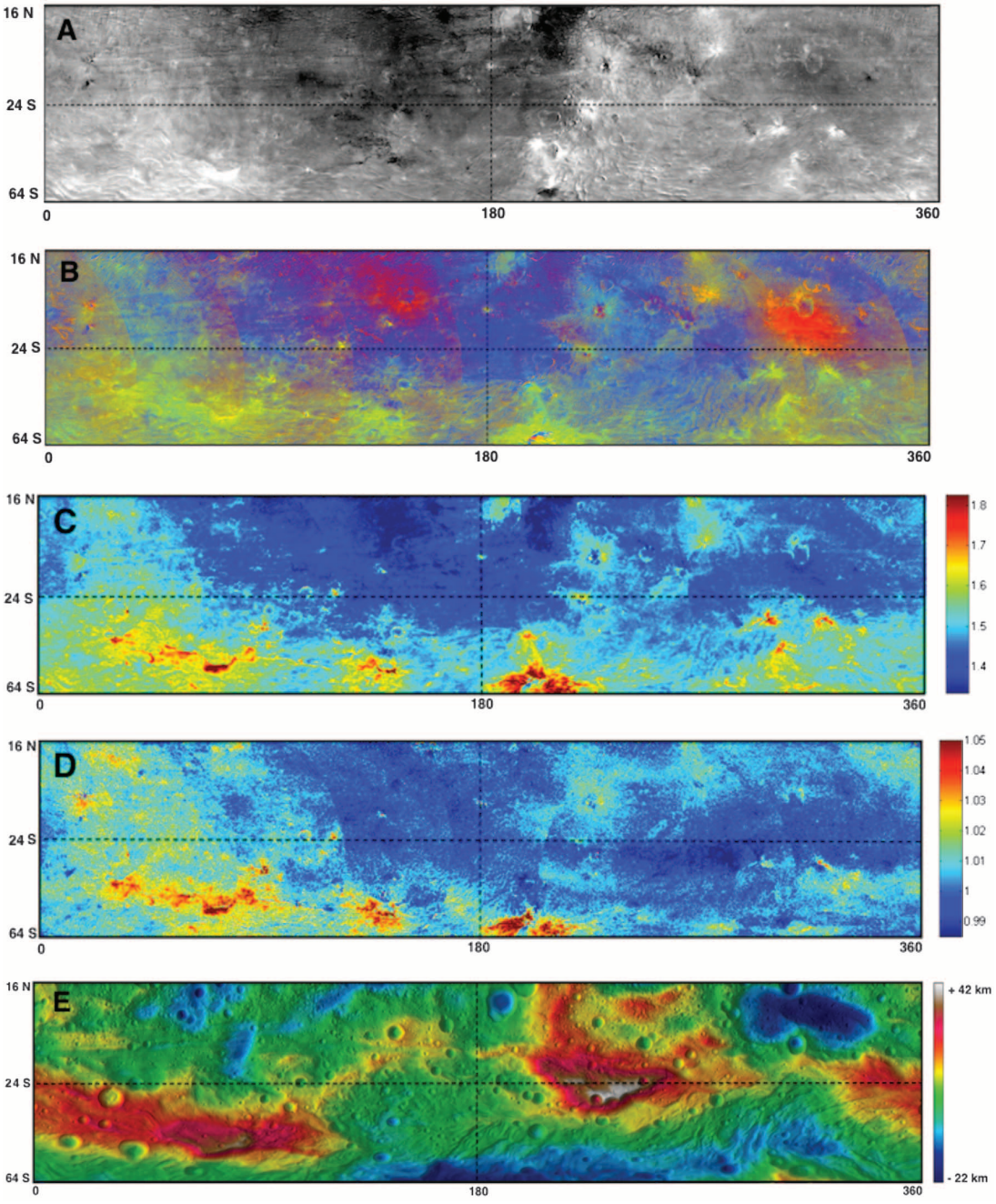

Fig. 1. Color mosaics of Vesta obtained during the approach phase (~480 m/pixel) in simple cylindrical projection. (**A**) Photometrically corrected 0.75-μm filter global mosaic showing east-west and north-south dichotomies in reflectance. (**B**) Clementine color ratios mosaic using $C_R = R(0.75)/R(0.45)$, $C_G = R(0.75)/R(0.92)$, and $C_B = R(0.45)/R(0.75)$, where $R(\lambda)$ is the reflectance in a filter centered at λ(micrometer) and C_R, C_G, C_B are the colors red, green, and blue, respectively. Greener areas have deeper bands, and redder areas have steeper visible slopes relative to bluer areas. (**C**) Rainbow-color coded map of $R(0.75)/R(0.92)$ ratio (proxy for 0.90-μm pyroxene band depth) showing areas with deeper bands as red. (**D**) Rainbow-color coded map of $R(0.98)/R(0.92)$ ratio (Eucrite-Diogenite) showing diogenite-rich regions as red and eucrite-rich regions as blue (*8*). (**E**) Color-shaded topographic map of Vesta with white corresponding to the highest elevation and blue the lowest. Minimum and maximum elevations are computed relative to a 285- × 229-km reference ellipsoid. All maps are based on the new Claudia coordinate system, which is different from the older Olbers system used with the Hubble Space Telescope data. Olbers reference longitude is located approximately at 210°E in the Claudia system.

align the seven color frames in order to create color cubes before analysis.

Global maps show variations in 0.75-μm albedo (Fig. 1A) and the 0.90-μm pyroxene absorption depth $R(0.75)/R(0.92)$ (Fig. 1C). The ratio $R(0.98)/R(0.92)$ qualitatively identifies eucrite- and diogenite-rich terrains (Fig. 1D). All of these features show a weak relation to topography (Fig. 1E). A false color composite quantifies band depth and visible slope (Fig. 1B). Because eucrites have more ferroan pyroxene than diogenites (fig. S1), their 0.90-μm pyroxene band is shifted toward longer wavelength (fig. S2) (*8*, *9*), causing the $R(0.98)/R(0.92)$ to be closer to 1 for eucrites but higher for diogenites (Fig. 1D). We further confirmed the compositional identification of specific color units with laboratory spectra of HED meteorites using several spectral criteria (*10*).

The maps (Fig. 1, A to E) reveal a hemispherical scale dichotomy on Vesta. The brightest point (in clear filter) is on a crater wall near the south pole that has a SSA of ~0.82 and a geometric albedo of ~0.67; the darkest area has a SSA of ~0.15 and a geometric albedo of only ~0.10. This range is much higher than is seen in other asteroids (*8*). The global albedo map also exhibits an overall lower reflectance in the eastern hemisphere as compared with the western (*3*, *11*). The area located between 30°S and the Rheasilvia Formation at the south pole also has higher albedo as compared with that of the northern hemisphere (Fig. 2, A and B). In addition, two distinct lower albedo units are associated with the ejecta of the Marcia (10°N, 190°) and Oppia (8°S, 309°) impact craters.

This dichotomy reflects both Vesta's composition and regolith processes. Abundance of mafic minerals (iron abundance), space weathering, grain size, and presence of opaque minerals are known to affect the $R(0.75)/R(0.92)$ ratio (*8*). Laboratory study of HED meteorites suggests that grain size is a major cause for band depth dichotomy (*8*). Unlike the Moon, where the highland units have higher albedo as compared with those of lower and darker mare, Vesta does not seem to have distinct global correlation between topography and albedo or color.

Along with global color dichotomy, we have identified various terrains on Vesta that are further evidence for surface heterogeneity. We have classified these areas as bright, dark, gray, and orange terrains (Fig. 3, A to H). Fresh impact craters have higher reflectance (30 to 40% in the 0.75-μm filter) than that of background surface and are associated with bright terrains (such as the Canuleia crater) (Fig. 3, A and B). They also have deeper 0.90-μm pyroxene absorption band. In the south, several fresh craters appear redder in the eucrite/diogenite (ED) ratio maps, suggesting that diogenite-rich material was excavated within Rheasilvia. By comparing the color spectra of bright material with global average, we find that the $R(0.75)/R(0.92)$ ratio is 16% deeper, and the visible spectral slope (0.45 to 0.55 μm) is also steeper (Fig. 4, A and B).

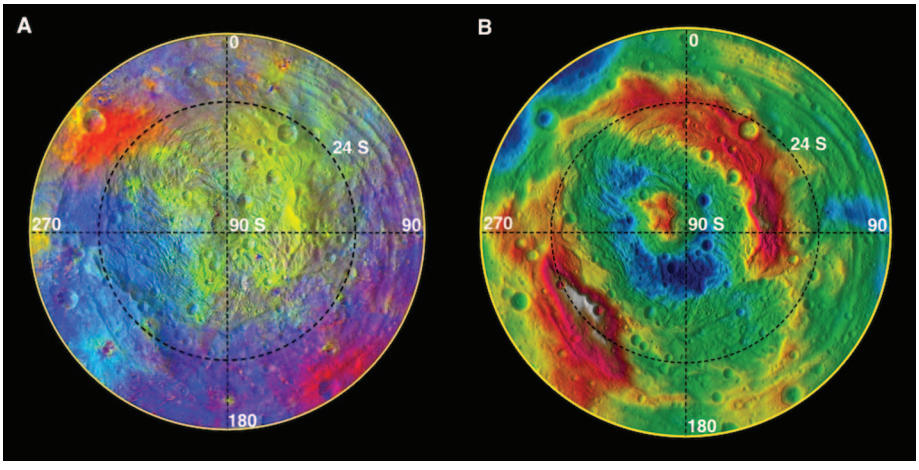

Fig. 2. Stereographic projection centered on the south pole of (**A**) the color mosaic in Clementine color ratios overlaid on a shaded-relief map and of (**B**) the color-shaded topographic map.

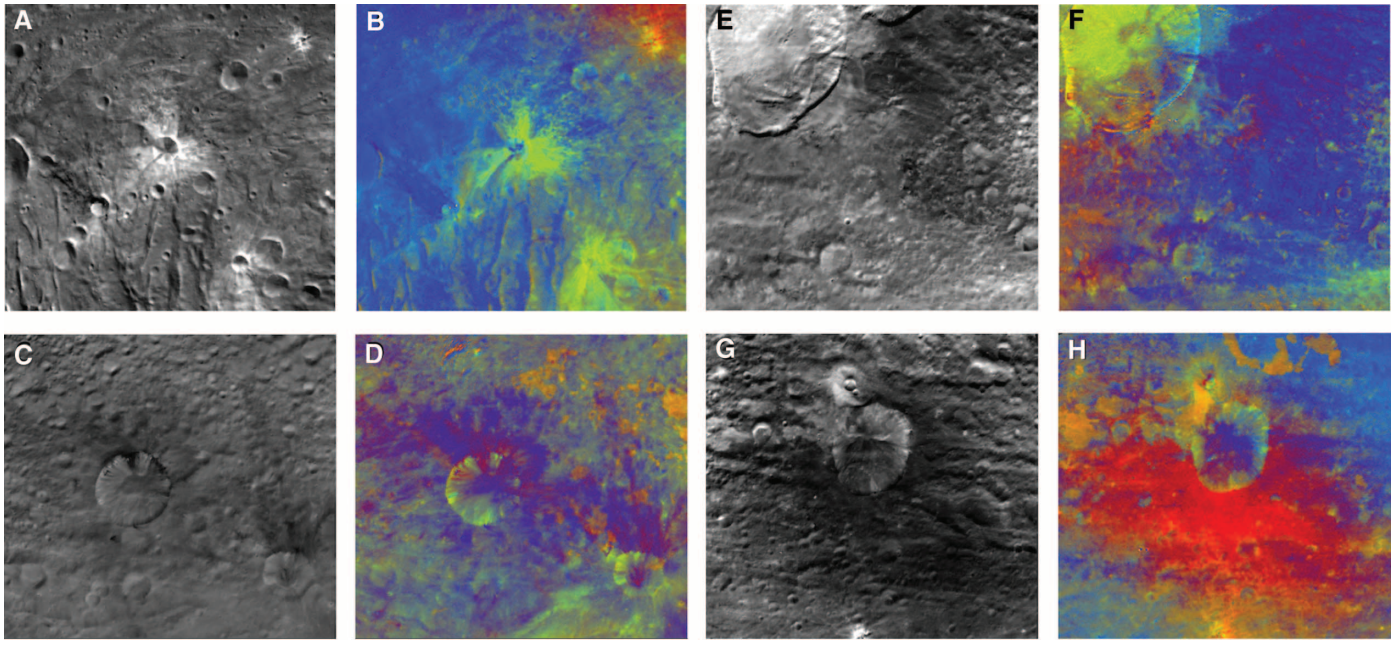

Fig. 3. Examples of diverse color terrains on Vesta in 0.75-μm filter (left) and Clementine ratio (right). (**A** and **B**) Bright ejecta around the 11.2-km diameter fresh impact crater Canuleia located at 33.7°S, 294.5°E. (**C** and **D**) Dark material on the crater wall and in the surroundings of the 30-km diameter Numisia crater located at 7°S, 247°E. (**E** and **F**) Gray ejecta blanket of the 58-km diameter Marcia crater (top left) located at 10°N, 190°E. (**G** and **H**) The 34-km diameter impact crater Oppia located at 8°S, 309°E, with orange ejecta blanket.

Dark material is commonly associated with impact craters (such as the Numisia crater) (Fig. 3, C and D), but dark deposits are also seen elsewhere in >25 locations. In some cases—Lucaria Tholus—dark material is associated with a topographic high. In addition, several fresh impact craters exhibit excavation of bright and dark material within the crater walls and ejecta blankets (Fig. 3, C and D). They have lower reflectance (8 to 13% at 0.75 μm), weaker band depth (Fig. 4, A and B) and have a redder visible spectral slope. Either the excavation of a darker subsurface layer or the incorporation of dark material by an impactor could explain the observed morphology of these units. The dark material on Vesta may indicate the presence of impact melts and exogenous carbonaceous material (*8*), both of which are seen in the HED meteorites.

Most of the surface of Vesta is covered with gray material (0.75-μm reflectance, ~15 to 30%). This material has a moderate $R(0.75)/R(0.92)$ ratio (Fig. 4, A and B). In craters, downslope movements have unveiled underlying bright material. Hence, gray material could correspond to a mixture of bright and dark material or space-weathered bright material. Space weathering affects optical properties of the regolith of planetary bodies without an atmosphere. A second type of gray material is associated with ejecta blankets around large impact craters such as the Marcia crater (Fig. 3, E and F) and is possibly impact melt. This gray material has a 0.75-μm reflectance of ~15%, a shallow visible slope, and the second weakest $R(0.75)/R(0.92)$ ratio (Fig. 4, A and B).

The Oppia crater displays asymmetric orange ejecta in the Clementine ratio map (Fig. 3, G and H) that is spread toward the southeast. The morphology of Oppia could be explained by an oblique impact or an impact on a slope. This particular unit has a steep visible spectral slope (redder in Clementine ratios) and a weak $R(0.75)/R(0.92)$ ratio; thus, it has a shallower 0.90-μm pyroxene band as compared with the global mean spectrum (Fig. 4, A and B). Several lighter "orange patches" are also observed to the west and north around Oppia (Fig. 3, G and H).

Band depth and ED maps (Fig. 1, C and D) show that areas with deeper $R(0.75)/R(0.92)$ ratios also tend to have higher $R(0.98)/R(0.92)$ ratios (*8*). This correlation suggests that diogenite-rich material has a deeper $R(0.75)/R(0.92)$ ratio as compared with that of eucrite-rich material. Terrains with higher ratios surround Rheasilvia basin in the south, whereas Vesta has lower ratios in the north (Fig. 1, C and D). The observed variance is consistent with diogenite-rich terrains (red) in the south and more eucritic terrains (blue) in the north, which is in agreement with Visible and Infrared Imaging Spectrometer observations (*12*). This north-south dichotomy is disrupted by a swath (~0 to 90°E) of relatively higher $R(0.75)/R(0.92)$ and $R(0.98)/R(0.92)$ ratio material that protrudes to the northern extent of Dawn's observations (Fig. 1, C and D). This swath is probably impact ejecta from the Rheasilvia forming event because it is topographically higher than adjacent terrains (Fig. 1E) and has similar $R(0.75)/R(0.92)$ and $R(0.98)/R(0.92)$ ratios to Rheasilvia material (Fig. 1, C and D). Also, meteoritical evidence suggests that diogenitic material probably formed deep beneath the surface of Vesta (*13*). The central peak of the Rheasilvia basin has a strong $R(0.75)/R(0.92)$ ratio (Fig. 2A), implying that it is dominated by material with a strong 0.90-μm pyroxene band (diogenite-rich).

The high rim of Rheasilvia (Figs. 1, C and D, and 2, A and B) is dominated by high $R(0.75)/R(0.92)$ and $R(0.98)/R(0.92)$ ratio material, which is consistent with diogenite-rich rocks that have been excavated from depth and deposited as ejecta. However, the abundance of deeper-band material is not homogeneous along the entire Rheasilvia rim. The eastern portion, between ~0 and 130°E, has higher concentrations of high-band-ratio material than the western portion (210 to 300°E), which is consistent with the western portion containing relatively more eucritic material. The origin of this variation is not immediately clear. Given that the western portion of the rim is topographically higher (Figs. 1E and 2B), we would expect it to contain higher concentrations of diogenite material (ejecta), which it does not. This may be an indication that the western portion of the Rheasilvia ejecta rim sampled previously reworked lithologies, which may be linked to the large pre-Rheasilvia basin impact (*14*).

Two localized concentrations of the highest $R(0.75)/R(0.92)$ and $R(0.98)/R(0.92)$ ratio material occur in areas associated with Rheasilvia (Figs. 1, C to E, and 2, A and B). The first (43 to 55°S, 51 to 87°E) coincides with a large scarp face, possibly indicating diogenite-rich material exposed along the rim and wall of the basin, and deposited nearby in the ejecta material. The second location (53 to 64°S, 180 to 230°E) is at a topographical low in the Rheasilvia basin floor and corresponds to the Antonia crater and its associated ejecta. Given the likely depth of excavation and the high-band-ratio signature, this material may be an in situ diogenitic lithology that has been exposed by the Rheasilvia impact event.

In a magma ocean model, a single, deep-seated layer of diogenitic material is expected (*15*), and if this region in the Rheasilvia basin is the only region with in situ diogenite material identified on Vesta, a magma ocean model may be favored. Our analyses show that Vesta was large enough to accrete material and differentiate during the first few million years of Solar System formation. Although battered by multiple impacts, Vesta remains intact today probably because of its differentiated internal structure. These catastrophic events have not only excavated deeper

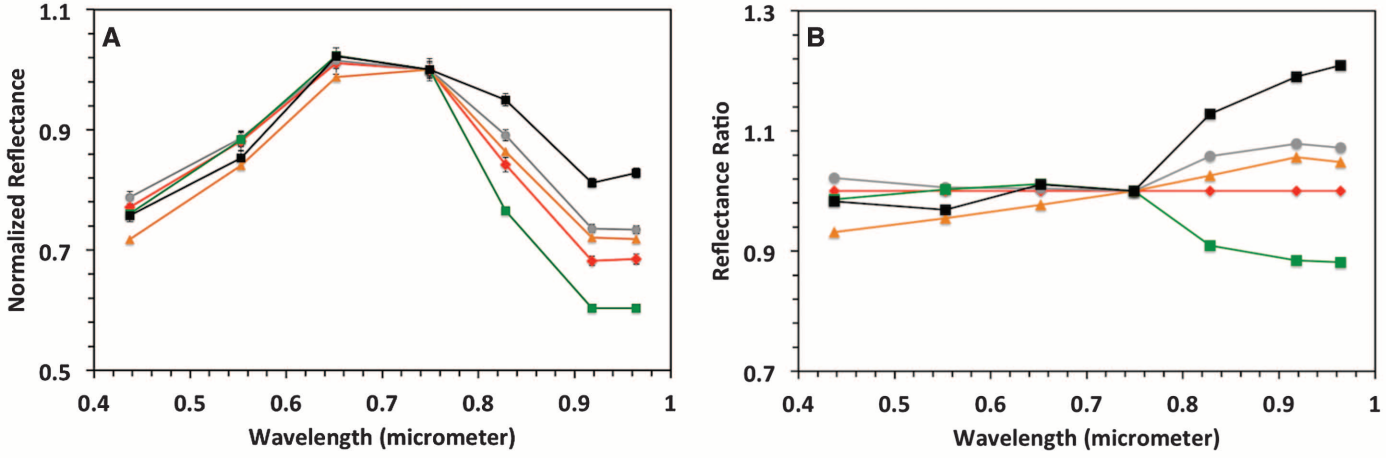

Fig. 4. (**A**) Color spectra of bright (green), dark (black), gray (gray) and orange terrains (orange) on Vesta. The red spectrum corresponds to the global average spectrum of Vesta. Errors shown are 1σ. (**B**) Ratios of the same color spectra divided by the global average spectrum (red). Dark, gray, and orange terrains have weaker $R(0.75)/R(0.92)$ ratios, whereas bright material has deeper ratio as compared with the global average. The orange ejecta exhibits the steepest visible slope with respect to global average.

compositional units but also delivered exogenous carbon-rich material to Vesta, a key ingredient for the formation and evolution of life on Earth.

References and Notes

1. H. Sierks *et al.*, *Space Sci. Rev.* **163**, 263 (2011).
2. K. Keil, in *Asteroid III*, William F. Bottke, Alberto Cellino, Paolo Paolicchi, Richard P. Binzel, Eds. (Univ. of Arizona Press, Tucson, 2002), pp. 573–584.
3. P. C. Thomas *et al.*, *Icarus* **128**, 88 (1997).
4. T. B. McCord, J. B. Adams, T. V. Johnson, *Science* **168**, 1445 (1970).
5. G. J. Consolmagno, M. J. Drake, *Geochim. Cosmochim. Acta* **41**, 1271 (1977).
6. J. Wisdom, *Nature* **315**, 731 (1985).
7. R. P. Binzel, S. Xu, *Science* **260**, 186 (1993).
8. Materials and methods are available as supplementary materials on *Science* Online.
9. M. J. Gaffey, *J. Geophys. Res.* **81**, 905 (1976).
10. L. Le Corre, V. Reddy, A. Nathues, E. A. Cloutis, *Icarus* **216**, 376 (2011).
11. J.-Y. Li *et al.*, *Icarus* **208**, 238 (2010).
12. M. C. De Sanctis *et al.*, *Science* **336**, 697 (2012).
13. D. W. Mittlefehldt *et al.*, *Planet. Mat.* **36**, 4-1 (1998).
14. P. Schenk *et al.*, *Science* **336**, 694 (2012).
15. A. Ruzicka, G. A. Snyder, *Meteor. Planet. Sci.* **32**, 825 (1997).

Acknowledgments: We thank the Dawn team for the development, cruise, orbital insertion, and operations of the Dawn spacecraft at Vesta. The Framing Camera project is financially supported by the Max Planck Society and the German Space Agency, DLR. We also thank the Dawn at Vesta Participating Scientist Program for funding the research. A portion of this work was performed at the Jet Propulsion Laboratory, California Institute of Technology, under contract with NASA. Dawn data are archived with the NASA Planetary Data System.

Supplementary Materials

www.sciencemag.org/cgi/content/full/336/6082/700/DC1
Materials and Methods
Figs. S1 and S2
References (*16*–*31*)

13 January 2012; accepted 13 April 2012
10.1126/science.1219088

Coupling Quantum Tunneling with Cavity Photons

Peter Cristofolini,[1] Gabriel Christmann,[1] Simeon I. Tsintzos,[1,2] George Deligeorgis,[2]* George Konstantinidis,[2] Zacharias Hatzopoulos,[2] Pavlos G. Savvidis,[2,3] Jeremy J. Baumberg[1]†

Tunneling of electrons through a potential barrier is fundamental to chemical reactions, electronic transport in semiconductors and superconductors, magnetism, and devices such as terahertz oscillators. Whereas tunneling is typically controlled by electric fields, a completely different approach is to bind electrons into bosonic quasiparticles with a photonic component. Quasiparticles made of such light-matter microcavity polaritons have recently been demonstrated to Bose-condense into superfluids, whereas spatially separated Coulomb-bound electrons and holes possess strong dipole interactions. We use tunneling polaritons to connect these two realms, producing bosonic quasiparticles with static dipole moments. Our resulting three-state system yields dark polaritons analogous to those in atomic systems or optical waveguides, thereby offering new possibilities for electromagnetically induced transparency, room-temperature condensation, and adiabatic photon-to-electron transfer.

Strong coupling of photons to the interband exciton transition in a semiconductor microcavity leads to the formation of polaritons, bosonic quasiparticles whose properties are governed by their mixed light-matter composition. Owing to their quantum indistinguishability and the interplay of their Coulomb interactions, microcavity polaritons show unusually strong light-matter interactions and many-body quantum effects. In particular, their small effective mass allows observation of quantum degeneracy effects at temperatures from 10 to 300 K, such as Bose condensation (*1*–*4*) and superfluidity flow dynamics (*5*), and their tunable interactions make them ideal candidates for future quantum optoelectronic devices (*6*) working at room temperature (*7*). By contrast, spatially separating the electrons and holes in coupled double quantum wells yields indirect excitons with sufficiently long lifetimes for thermalization and a large static dipole moment (*8*). These properties enable efficient in-plane electrostatic traps (*9*, *10*) and the coherent control of electron spins (*11*). By embedding double quantum wells inside a conventional microcavity in the strong coupling regime, we unite the concepts of indirect excitons and microcavity polaritons to produce optically active quasiparticles with transport properties, named dipolaritons. These offer the advantages of both systems: electrical trapping and tuning of excitons, strong optical coupling to low-mass quasiparticles with large de Broglie wavelength, and excellent control over the dipole properties and interactions (*12*, *13*).

Microcavities are formed from p-i-n semiconductor multilayers surrounded by doped multilayer mirrors (*7*) (Fig. 1A; details in the supporting online material) and pumped with a nonresonant laser. Quantum wells (QWs) of InGaAs inside the cavity are arranged in asymmetric pairs separated by a thin barrier (of width L_B) that allows electrons to tunnel between the two wells (Fig. 1A). Because of the large effective hole mass and the wide energy separation of hole levels in neighboring QWs, hole tunneling is negligible, and only the low-energy left QW (LQW) hole state is considered. Without tunneling, there are two types of exciton in this system. The direct exciton $|DX\rangle$ has both electron and hole in the left QW (Fig. 1B, top) and therefore strongly couples to the cavity mode, with its induced dipole moment oriented randomly in the QW plane. The indirect exciton $|IX\rangle$ has the hole in the left QW and the electron in the right QW—thus possessing an additional static dipole moment aligned perpendicularly to the plane—and has a very small overlap of electron and hole wave functions, hence low oscillator strength. When a bias voltage is applied to bring the electron levels into resonance, the electron states in the two QWs mix to give symmetric and antisymmetric electron wave functions (red in Fig. 1A), which, together with the low-energy hole states (blue) in the left QW, produce the exciton modes $(1/\sqrt{2})\{|IX\rangle \pm |DX\rangle\}$, split by the tunneling energy $\hbar J$ (where $\hbar$ is Planck's constant divided by 2π). These modes combine the large oscillator strength of the DX with the large static dipole moment of the IX (Fig. 1B, bottom).

Embedding DX and IX excitons in the microcavity with cavity mode C now forms a three-state system similar to the atomic Λ-scheme (*14*, *15*), which is coupled optically by the vacuum Rabi frequency Ω and electronically by the electron tunneling rate J (Fig. 1C). Although J and Ω are intrinsic to the microcavity design, full control of the dipolariton modes is possible through bias voltage control of tunneling and angle tuning of the cavity mode. In the strong coupling regime, when J is larger than the carrier escape rate from the coupled QWs and Ω is faster than the photon decay rate, the system displays three distinct eigenmodes: the lower (LP), middle (MP), and upper (UP) dipolaritons. Thus, a conventional microcavity polariton (Fig. 1D, black) can be simply bias-tuned to yield the dipolariton spectrum (red) in the strong tunneling regime.

The bias dependence of the photoluminescence (PL) of a mesa with barrier width L_B = 4 nm (Fig. 2) clearly reveals these three dipolariton modes. Because in-plane wave vectors k are conserved, photons emitted at an angle θ directly measure dipolaritons at k. At normal incidence (Fig. 2, A and C) the narrow cavity mode is detuned below the excitons, whereas at 35° (Fig. 2, B and D) the uncoupled modes are all degenerate. For higher electric fields, the PL emission weakens because electrons escape the coupled QW system before they can recombine radiatively with a left QW hole, and eventually two of the modes vanish, leaving only the most cavity-

[1]NanoPhotonics Centre, Cavendish Laboratory, University of Cambridge, Cambridge CB3 0HE, UK. [2]FORTH-IESL, Post Office Box 1527, 71110 Heraklion, Crete, Greece. [3]Department of Materials Science and Technology, University of Crete, Post Office Box 2208, 71003 Heraklion, Greece.

*Present address: CNRS, LAAS, 7 avenue de Colonel Roche, F-31077 Toulouse Cedex 4, France.

†To whom correspondence should be addressed. E-mail: jjb12@cam.ac.uk